

Full length article

The effect of defects on the mechanical response of Ti-6Al-4V cubic lattice structures fabricated by electron beam melting



E. Hernández-Nava^{a,*}, C.J. Smith^a, F. Derguti^a, S. Tammam-Williams^b, F. Leonard^c, P.J. Withers^b, I. Todd^a, R. Goodall^a

^a Department of Material Science & Engineering, The University of Sheffield, Sir Robert Hadfield Building, Mappin St, Sheffield S1 3JD, UK

^b Henry Moseley X-ray Imaging Facility, School of Materials, The University of Manchester, M13 9PL, UK

^c Bundesanstalt für Material for schung und –prüfung (BAM), Unter den Eichen 87, 12205 Berlin, Germany

ARTICLE INFO

Article history:

Received 16 October 2015

Accepted 11 February 2016

Keywords:

Cellular solids

Additive manufacturing

Titanium alloy

Mechanical properties

X-ray computed tomography

ABSTRACT

Electron Beam Melting (EBM) as a means of Additive Manufacturing (AM), is of interest for the fabrication of intricate geometries for cellular materials in areas where complex architectures are needed, e.g. biomedical implants. Most studies have focused on specific geometries and so the effect of the structure on mechanical performance is not well understood. Many kinds of micro- and macro-scale defects can arise in additively manufactured components, so assessment of their influence on properties is needed. In this work, lattices of Ti-6Al-4V having a cubic structure have been manufactured by EBM, and the effect of heat treatments above and below the β -transus temperature on microstructure and compression response have been investigated. The former modifies only slightly the $\alpha + \beta$ structure and mechanical performance whereas the latter leads to coarse alternating α and β lamellae packets and α at the prior grain boundaries with a 10% loss in yield strength. The variation in the compressive yield stress with strut diameter is in good accord with simple models based on compressive deformation rather than shearing or buckling. Internal pores for struts aligned with the build direction are found around the edges of the solid form, in regions which seem to be associated with the EB scan pattern. Struts normal to the build direction show more significant defects but their redundancy means that they do not compromise the compressive performance in the build direction. Using a particle size in the range 45–100 μm minimum weld-track sizes were experimentally and numerically identified to be 176 and 148 μm in depth respectively with a depth-to-width ratio of 0.55. This produced a beam pass of the order of 300 μm oversizing small features (struts of 0.4 and 0.6 mm nominal diameter) when a contour around the strut periphery was applied.

© 2016 Acta Materialia Inc. Published by Elsevier Ltd. This is an open access article under the CC BY license (<http://creativecommons.org/licenses/by/4.0/>).

1. Introduction

Lattice or micro-truss materials prepared by additive manufacturing (AM) have attracted interest due to the prospect of tailoring properties by the selection of different topologies. These structures belong to the class of materials known as cellular solids which comprise an interconnected network of struts or membranes [1]. These structures have been studied by x-ray imaging techniques [2] to characterise their structural configuration in three dimensions (3D) enabling relationships such as Eq. (1) [3] for the failure strength, σ^* , in terms of the relative density, ρ_r , and parent

material strength, σ_s :

$$\sigma^* = C\sigma_s\rho_r^{3/2} \quad (1)$$

to be evaluated where C a constant of proportionality (varying from 0.1 to 1 for metal foams [4]). In contrast to other cellular solids, lattice structures are often observed to fail dramatically and cooperatively due to the layer configuration [5]. This makes the failure strength more difficult to identify than in foams where there a clear plateau stress is common. Although there is no general rule to identify maximum strength prior failure, common practice is to define the failure strength as the intersection with the curve of a line matching the slope of the linear section at an offset strain [6]. Here in this work this method was used with an offset of 0.2%.

It is well known that structural predictions using models as

* Corresponding author.

E-mail address: mtq10eh@sheffield.ac.uk (E. Hernández-Nava).

the previously mentioned may not be accurate due to the variation of exponents and constants as the geometry changes. Additionally, structural models may underestimate the integrity of solid parts by not taking into account process features giving structures which do not meet the ideal assumptions, having internal porosity or being undersized [7]. In this context it should be recognised that there is often a disparity between the intended structural design and that achieved in practice. For example, volumetric defects are often present [8] and wall/strut thicknesses and geometries are not always faithfully reproduced due to manufacturing constraints. Furthermore for metallic lattices the microstructure arising from AM may be very different from that characteristic of the bulk alloy. From a performance optimisation viewpoint it is essential that these process related issues are well understood. Previous work [6] has shown that morphological defects in the struts and a lower intrinsic strength of the alloy as additively manufactured over that for the bulk are responsible for a significant decrease in matrix strength as the relative density of the lattice is decreased. This work suggests that the probability and influence of defects becomes higher as the strut dimensions are refined in scale however, the level of defects introduced is strongly related to the material deposition strategy [9] and thus indirectly also to the material being processed.

Up until now much of the focus of research has been on the instrumentation associated with additive manufacturing and its control. Further research on the effect of material deposition strategies and the influence of alloy microstructure is needed in order to optimize the structural performance of EBM components [10]. Consequently we have investigated the sensitivity of the compressive performance to defects in EBM scaffold structures. This is coupled with an investigation of the effect of alloy condition on properties comparing “as-built” and homogenized Ti-6Al-4V microstructures achieved by heat treatments above and below the β -transus temperature. In addition an analytical approach has also been developed to compare results with expectations.

2. Experimental procedure

2.1. Structure design

A cubic unit cell (Fig. 1a) was designed in Netfabb® and replicated to generate a $4 \times 4 \times 4$ cell 3D lattice structure (Fig. 1b). An octagonal cross-sectional profile was used to define each strut (Fig. 1c), which can be described with a relatively low number of triangles in the STL (Standard Tessellation Language) file, while aiming for a circular shape of a cylinder to be produced. The STL file (Fig. 1d) was then converted into 2D as “sliced” files for manufacturing purposes. Four different strut diameters were used; 0.8, 1, 1.5 and 1.8 mm each with a 5 mm unit cell size (a $20 \times 20 \times 20$ mm sample).

The calculations to determine the relative density of the designed structures were therefore based on the smallest repeating element, being the ratio of solid volume, V_s , for three intersecting cylinders within the volume of a unit cell, V_u , shown in Fig. 1a and Eq. (2).

$$\rho_r = \frac{V_s}{V_u} = \frac{3V_c - 3V_{I2} + V_{I3}}{\beta^3} = \left(\frac{d}{l}\right)^2 \left[\frac{3\pi}{4} - \frac{d\sqrt{2}}{l} \right] \quad (2)$$

where V_c , V_{I2} and V_{I3} are the volumes of a cylinder of length l and diameter d , the intersection of two cylinders and the intersection of three cylinders respectively.

2.2. Manufacturing

2.2.1. EBM processing and raw material

The raw material comprised spherical Ti-6Al-4V prealloyed powder (Al 6.49, V 4.05, C 0.02, Fe 0.21, O 0.252, N 0.037 in wt%) of 45–100 μm particle size. The EBM process was set up to deposit layers of 70 μm in thickness. In each layer, the powder was first preheated with a defocused beam, using a sequence of 10 passes across the build envelope (‘preheat’ setting in Table 1). The material deposition process comprised a “hatching” step and three consecutive “contours” (‘Net’ setting in Table 1). While the hatching (a continuous filling process) started at an offset of 0.05 mm from the CAD contour, the contouring (three consecutive “rings”) started with an offset of 0.15 mm from the CAD contour and 0.1 mm offset from each other. Such an arrangement, if optimized, is intended to melt the entire area while avoiding unmelted powder and over/under sizing. The beam offset, is intended to account for the size of the melt pool, intrinsically defined by the beam power and the material response to the incoming electrons. From electron beam theory [11,12], it is known that the melt pool penetration is, among other factors, a function of the beam parameters of speed and power given in Table 1. It is critical then to identify the optimal electron beam parameters and offsets, especially for thin components, in order to achieve the desired resolution. However, it should be noted that melting micro-sections of the order of a few spherical particles would leave an intrinsic defect fraction due to the part size and shape relative to the powder size. This could take the form of interstices and severe roughness. In this investigation, all samples were fabricated using the same offset and electron beam parameters, and were tested in a direction parallel to the build orientation, leaving the strut diameter as the only variable.

2.2.2. Fabricated samples

18 lattice samples were manufactured for compression testing: 12 (3 of each strut thickness) for testing in the “as-built condition” (i.e. with no further heat treatment) and 6 (of 1.5 mm strut thickness) were heat treated. In addition, 9 ($66 \times 16 \times 16$ mm) cuboidal samples were made from which tensile bars were machined. The samples were fabricated using the same titanium powder as used for the lattices, but using the EB ‘Melt’ settings described in Table 1 tailored for the processing of larger samples without the requirement to produce fine features accurately. The ‘Melt’ setting employed a faster speed and increased beam power with no contours included.

In order to investigate the occurrence of different defects in the material at various diameter sections, single strut or “rod” samples were produced in a vertical orientation each representing a single structural element representative of the loaded lattice members. The processing and beam parameters were the same as those employed for the lattice samples, Table 1. These samples, S1 to S7, were designed to be 0.4, 0.6, 1, 1.2, 1.5, 1.8 and 2 mm in diameter.

Additionally, a set of 18 diamond-like lattice samples were manufactured for comparison. Their geometry was designed to have the same geometric relationship as the interatomic bonds in the diamond crystal structure (strut elements orientated at 109.5° from each other) of relative density 0.2, 0.4, 0.10, 0.11, 0.18, and 0.24. Such samples were manufactured to highlight the differences in mechanical response from cubic lattices only, leaving their characterisation to be analysed in a further communication.

2.3. The effect of thermal treatment

Three thermal treatments were explored; “as-manufactured”, heat treated high in the $\alpha + \beta$ region and heat treated above the β -transus temperature. The temperature profiles of the heat

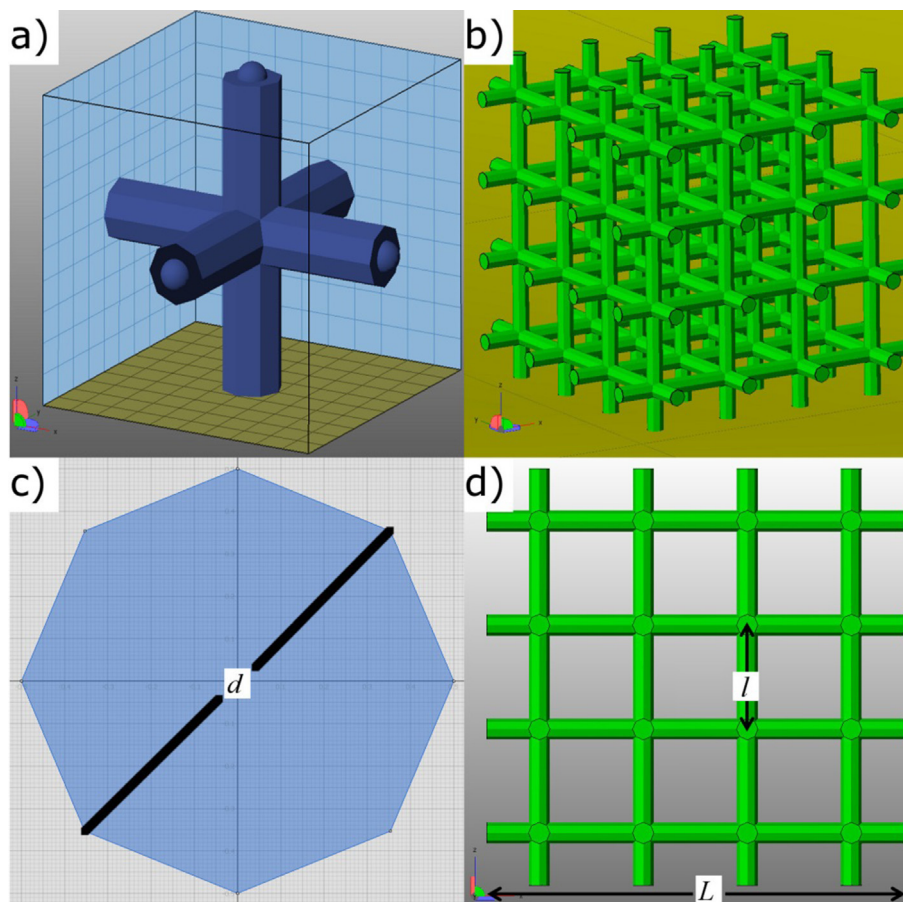


Fig. 1. a) Unit cell designed as the minimum repeatable symmetric unit, b) Scaffold comprising $4 \times 4 \times 4$ unit cells, c) Cross-section of a strut represented as an octagon of diameter “ d ”, d) frontal view of the scaffold showing the sample dimension, L , used to calculate compressive stresses.

treatments (which were carried out under high vacuum) comprised a heating rate of $10\text{ }^{\circ}\text{C}/\text{min}$ to $960\text{ }^{\circ}\text{C}$ or $1200\text{ }^{\circ}\text{C}$ for 2 h followed by furnace cooling (FC). The former ($960\text{ }^{\circ}\text{C}/2\text{ h}/\text{FC}$) was designed to retain the columnar β grain microstructure. It is reported that during heat treatments in the $\alpha + \beta$ region the α phase can be altered without a significant effect on prior β grains [13]. The latter ($1200\text{ }^{\circ}\text{C}/2\text{ h}/\text{FC}$), which is not usually applied to bulk Ti-6Al-4V, was intended to break down the columnar β grain shape typical of EBM components [14]. Such a microstructure forms because of the directional formation of the specimens and the preferred growth direction of the material.

While the cuboidal samples were machined into tensile specimens after the heat treatments, whereas the heat treated lattice samples were compressed without any further processing. Once machined, the tensile specimens were sent to Special Testing LTD, Sheffield, UK, and tested according to ASTM E8 standard to obtain the 0.2% Yield Strength, Ultimate Tensile Strength, elongation and

Young's Modulus data summarised in Table 3.

2.4. Mechanical evaluation

The lattices were tested in compression along the EBM build direction at room temperature, at an initial strain rate of $4.4 \times 10^{-4}\text{ s}^{-1}$ in a Zwick/Roell Z050 test rig machine. Stress-strain curves were corrected for the machine compliance and the 0.2% yield strength determined. Additionally, the Vickers microhardness (HV) was obtained using a Struers Durascan 70 automated system, using a standardized ASTM speed approach (0.1 kg load and 10s dwell time).

2.5. X-ray computed tomography

X-ray Computed Tomography (CT) was applied to the single strut samples to quantify the occurrence and distribution of various types of defect. The CT scanning was conducted at the Henry Moseley X-ray Imaging Facility in Manchester on a Nikon Metrology 225/320 kV Custom Bay machine. The custom bay system was equipped with a 225 kV static multi-metal anode source (Cu, Mo, Ag, and W) with a minimum focal spot size of $3\text{ }\mu\text{m}$ and a Perkin Elmer 2000×2000 pixels ($200\text{ }\mu\text{m}$ pitch) 16-bit amorphous silicon flat panel detector. Scanning was performed with a molybdenum reflection target using an accelerating voltage of 85 kV, a current of $125\text{ }\mu\text{A}$ and an exposure time of 2 s per projection. The beam was filtered with 0.25 mm of Cu to remove

Table 1

Main electron beam parameters for Ti-6Al-4V lattices and solid monoliths summarised as “Net” and “Melt” settings respectively.

Setting	Speed (mm/s)	Current (mA)	Focus offset (mA)	Contour offset (mm)
Preheat	14,600	25	50	—
NetHatch	200	1.7	0	0.05
Contour	200	1.7	0	0.15
Extra contours	200	1.7	0	0.1
Melt	500	17	19	0

Table 2
Comparison between specified and observed strut diameters and relative density for the “as-manufactured” cubic lattices. The uncertainties are estimated based on the standard deviation from each batch of samples.

Batch	Number of samples	Strut diameter (mm)			Relative density	
		STL	Sample		Analytical	Experimental
			Callipers	X-ray CT study		
1	3	0.8	0.81 ± 0.022	No data	0.05	0.063 ± 0.003
2	3	1	0.97 ± 0.023	0.88 ± 0.252	0.08	0.078 ± 0.004
3	9	1.5	1.48 ± 0.019	1.35 ± 0.223	0.17	0.159 ± 0.002
4	3	1.8	1.78 ± 0.028	1.65 ± 0.216	0.23	0.216 ± 0.005

low energy photons and avoid saturation of the detector. A geometrical magnification of 27 was achieved (giving an effective pixel size of 7.4 μm) by positioning the rods close to the conical beam x-ray source. 3142 equally spaced projections over 360° were taken, resulting in an acquisition time of approximately 108 min.

Reconstruction after the scan was performed with Nikon Metrology proprietary software CT-Pro. Segmentation of the reconstructed 3D image was carried out using Avizo 8 software and simple thresholding with the threshold value decided by the Otsu method [15]. Only pores consisting of more than 5 voxels were included in the analysis to exclude any noise in the data. Consequently the minimum detectable pore size was approximately 15 μm. The length of each rod imaged and quantified was approximately 11 mm.

The scanned surfaces were analysed once again in parametric studies constructed in Rhinoceros® 5 and Grasshopper™. The data was obtained after importing and aligning the STL files of all representative surfaces for each strut diameter. The mean area, second moment of area and radius (distant vertex length defined in Fig. 1c) were quantified from virtual cross-sections taken every 70 μm along the 10 mm length of the rods. The radius was extracted at aligned points along the axial direction of the strut, Fig. 2, allowing a longitudinal profile to be obtained such that the roughness along the strut length could be obtained.

2.6. Microstructural and phase analysis

The cubic lattice was cut along the build direction (z axis) to observe the strut elements using a Struers Minitom precision machine with a diamond abrasive disc with a solution of 90% water and 10% of low foam Triethanolamine additive as a cooling medium. Then, all samples were hot mounted in a conductive Bakelite resin using a Buehler Simplimet 1000 automatic press with a programmed cycle at 290 bar comprising 2 min heating and 4 min cooling time. Grinding was carried out in a Tegramin-20 Struers preparation system using; water and a 9 μm grain size Diamet suspension. The samples were then polished immediately using 20vol% colloidal silica (6 μm) in 80vol% water. Finally, for better contrast, the samples were etched in Kroll's reagent for 10 s before observation in a Nikon eclipse LV150 microscope under polarized

Table 3
Lattice diamond features of unit cell size, specified strut diameter and experimental relative density.

Unit cell length (L) (mm)	Strut diameter (d) (mm)	Experimental relative density (ρr)
10	0.5	0.020 ± 0.0002
10	1.0	0.044 ± 0.0005
8	1.3	0.106 ± 0.0009
8	1.8	0.111 ± 0.0010
5	0.8	0.184 ± 0.0050
5	1.3	0.240 ± 0.0008

light. The phases present in the Ti-6Al-4V alloy were identified by X-ray diffraction (XRD) using a SIEMENS 3000 diffractometer with Cu K_α radiation.

3. Results and analysis

3.1. Additively manufactured samples

After the EBM process all unmelted powder particles were removed from the samples using compressed air. After cleaning, values of relative density (from measurements of lattice dimensions and mass) and strut diameter (using callipers) were taken and are summarised in Table 2. Fig. 3 shows an example of each type of lattice. Although AM was able to produce a faithful reproduction of the lattice designs, the strut dimensions differed from those specified. In almost all cases (see Table 2), undersized strut diameters were found, possibly due to the offset in the contour parameters not being optimal.

The effect of the mismatch in strut dimensions can be observed in the deviation of measured relative density from predictions for low densities. However, there are also departures where the actual density is lower than the predicted one. This can be an indication of

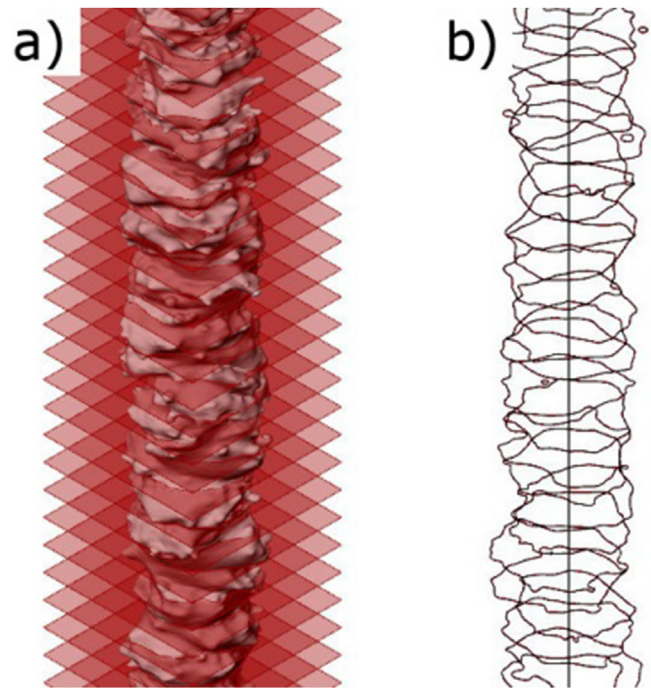


Fig. 2. Schematic illustration of the X-ray CT analysis of an imaged strut. (a) Virtual intersecting planes equally spaced were used to obtain the mean diameter and surface roughness along the EBM build axis, (b) The strut cross sections for the analysed sections.

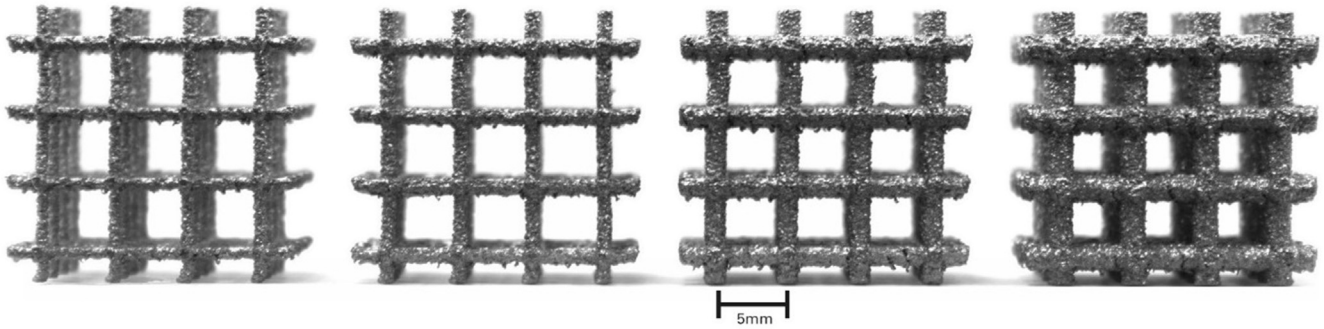


Fig. 3. EBM manufactured Ti-6Al-4V lattice samples with STL defined strut diameters of 0.8, 1, 1.5 and 1.8 mm (from left to right). The build direction is vertical.

a lack of solid volume throughout the lattice; the presence of holes for example. As the material added during the AM process has a tendency to collapse in unsupported areas, this unfilled volume may potentially be located in the horizontal struts of the lattices where such collapses are more likely. Conversely, vertical struts are expected to show a better integrity as the pre-deposited material is self-supportive.

A more precise measure of the strut diameter can be obtained from the results with CT scanned specimens also reported in Table 2. Only the struts from the previous study [6] which macroscopically had strut diameters coinciding with those designed are reported in this section. As can be seen no data are shown for struts designed to be 0.8 mm and only calliper measurements of these struts will be used for further analysis. Finally, the parameters for the fabricated diamond lattices built for comparison purposes are summarised in Table 3.

3.2. Microstructure

3.2.1. The “as-manufactured” condition

Optical micrographs of the as-manufactured samples are shown

in Fig. 4a. The deposited material showed a microstructure composed of columnar prior β grains parallel to the build direction (Fig. 4b). This orientation of the columnar morphology arises due to the maximum temperature gradient during solidification, going from the top of the component to the base plate for deposition. The decomposition products were identified as a basket-weave structure, observed in areas comprising the final deposited layers and close to sintered (i.e. unmelted but adhered) powder (Fig. 4c). Also, diffusionless α' -martensite (Fig. 4d) was identified in areas close to the start plate (bottom of Fig. 4a). These features have been reported previously for titanium alloys under similar solidification conditions [13]. This distribution seems to reflect different thermal conditions arising from the heat flux away from the electron beam to the start plate. This is not homogenous throughout the solidified material, as areas surrounded by sintered powder are more highly insulated than those close to the build start plate.

The formation of α' -martensite in EBM bulk components has been debated recently [14]. For lattice structures [16], it is related to the low thermal mass of the structure, leading to the transformation of martensite due to high cooling rates ($>410 \text{ K s}^{-1}$) above the martensite start temperature [17]. As the cooling rate for

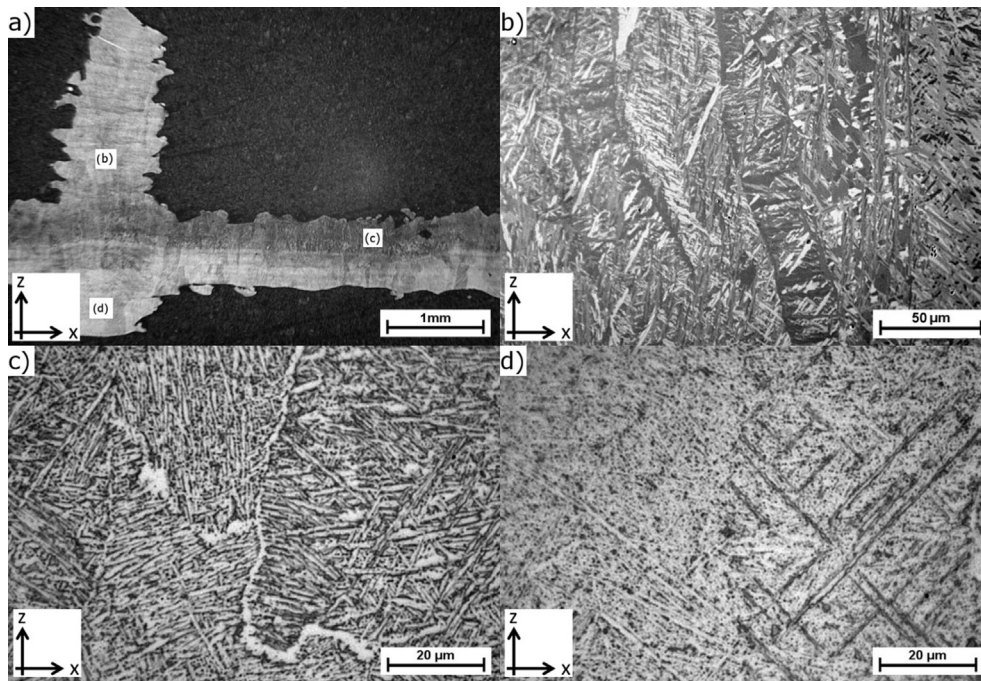


Fig. 4. a) optical micrograph of the “as-manufactured” bulk microstructure found in a sample from batch 3 (1 mm strut diameter), (the Z axis indicates the build direction) and three locations of interest b) the mid-height of a vertical strut showing columnar prior β grains, c) the top section of a horizontal strut having a characteristic $\alpha + \beta$ wave basket microstructure and d) a region close to the start plate where the EBM build begins showing diffusionless α' -martensite.

the powder-feed ALM process is up to 3500 K s^{-1} [18] the generation of α' -martensite is expected here as the cooling rates are anticipated to be comparable. The presence of α' -martensite is consistent with the XRD shown in Fig. 5a, however it is not possible to distinguish between α' and α in this technique as the peaks of α' share positions due to the same crystallographic structure.

Additional evidence for thermal mass comparisons came from observations on finer α within a basket-weave microstructure plate found on lattices than in the tensile samples microstructure, Table 4. This is the result of different cooling rates due to the difference in thermal mass between the lattice structures and the bulk blocks produced for fabrication of tensile samples. It is well known that the cooling rates in $\alpha + \beta$ titanium alloys from the β phase field determine the size of α laths and α colonies, although occurring at different ranges [13]. Previous investigations have shown drastic reductions of α lath size appears upon cooling rates of 1.66 K s^{-1} resulting in reductions from $5 \mu\text{m}$ to about $0.5 \mu\text{m}$ and further reductions to $0.2 \mu\text{m}$ for cooling rates up to 133 K s^{-1} [19]. Because of higher cooling rates experienced by lattice structures as mentioned earlier, it seems reasonable that the thickness of α laths found here are around $0.8 \mu\text{m}$. Because of this high cooling rate, further reductions in lath thickness would be difficult to achieve by thermal processing. This could be desirable because the microstructural scale is linked to mechanical properties. The hardness values of around 3.49 GPa found for the metal making up the lattice structures is in agreement with previous observations [20].

3.2.2. The $960^\circ\text{C}/2 \text{ h}/\text{FC}$ condition

It is clear from Fig. 6a and c that the microstructure is significantly modified by the $960^\circ\text{C}/2 \text{ h}/\text{FC}$ heat treatment. As mentioned previously, by heat treating in the $\alpha + \beta$ region we aimed to modify

the α -phase morphology without significantly changing the prior β phase grains. This is observed only in the lattice samples (Fig. 6a) as the observed plane from the tensile specimen is not precisely parallel to the build direction (Fig. 6c). A similar case is found for the tensile specimen heat treated at 1200°C shown in Fig. 6d and discussed in the next section.

In regard to the microstructure, X-ray diffraction suggests no significant crystallographic modification (Fig. 5b) while significant coarsening of the α phase morphology has occurred (Table 4). No significant fraction of α martensite could be found by optical microscopy which is consistent with the conversion of martensitic microstructure to lamellar $\alpha + \beta$ under annealing heat treatments applied in the high $\alpha + \beta$ temperature range [19].

The microstructural homogenization has had no significant effect on the microhardness relative to the as-manufactured condition (Table 4). This can be seen as a mechanically unchanged $\alpha + \beta$ microstructure from the “as-built” condition, although with a coarser α plate thickness. Additionally, the absence of martensite and the coarser microstructure size do not affect significantly the strength. The martensitic transformation is not a strengthening mechanism for titanium alloys in the same way as for steels [19], and this highlights that solid solution (interstitial or substitutional) is the main strengthening mechanism in this case. Therefore it can be concluded that both the similar phase contents and hardness in the as-manufactured material can be considered equivalent to the annealed material.

3.2.3. The $1200^\circ\text{C}/2 \text{ h}/\text{FC}$ condition

In contrast to the lower temperature heat treatment, heat treatments above the β -transus temperature drastically modify the microstructure. This is achieved through a degree of

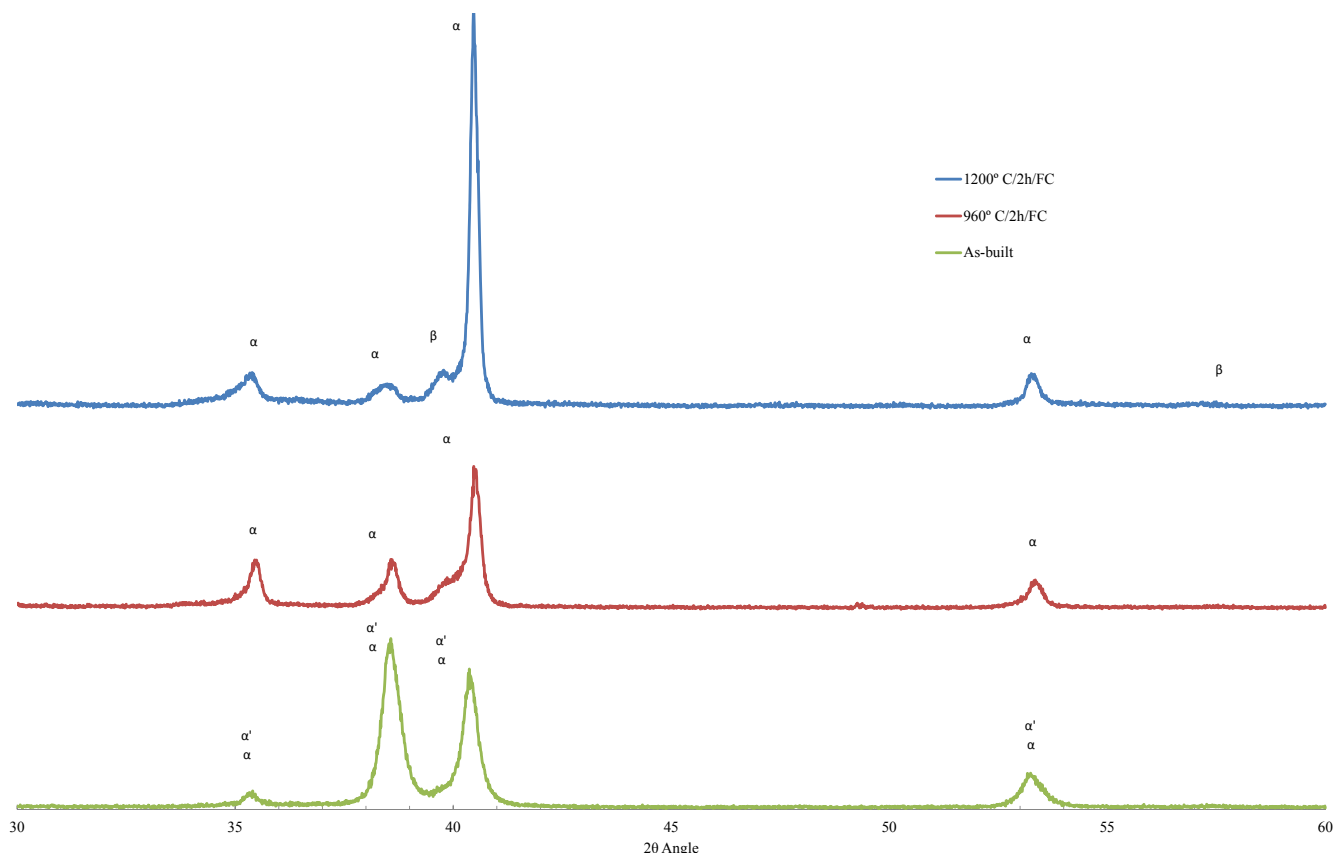


Fig. 5. X-ray diffraction profiles for Ti-6Al-4V lattice strut sections in; a) as manufactured EBM condition, b) $960^\circ\text{C}/2 \text{ h}/\text{FC}$ and, c) $1200^\circ\text{C}/2 \text{ h}/\text{FC}$ samples.

Table 4
Comparison of microstructural features and mechanical properties for the lattices and tensile samples in the three conditions under study.

Batch 3 condition	Lattice samples			Tensile samples		
	α -lath thickness (μm)	Vickers micro hardness (GPa)	0.2 YS (MPa)	α -lath thickness (μm)	Vickers micro hardness (GPa)	0.2 YS (MPa)
As-manufactured	0.9 ± 0.5	3.5 ± 0.1	88 ± 1	2.9 ± 0.9	3.5 ± 0.1	850 ± 13
960° C/2 h/FC	6.3 ± 1.5	3.5 ± 0.2	85 ± 2	4.1 ± 1.2	3.5 ± 0.1	865 ± 5
1200° C/2 h/FC	13.8 ± 1.1	3.1 ± 0.1	67 ± 9	9.2 ± 2.7	3.6 ± 0.2	783 ± 6

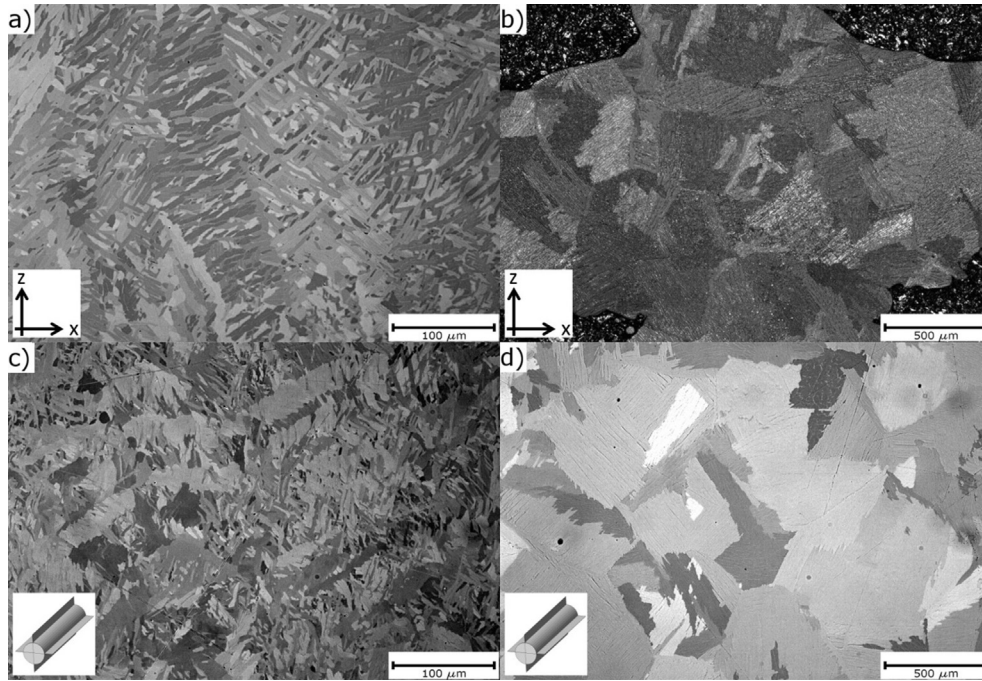


Fig. 6. Optical micrographs of the cubic lattice specimens, the Z axis indicates the build direction while the schematic representation indicates a different plane from the one parallel to the build direction. (a) 960/2 h/FC and (b) 1200/2 h/FC heat treatment. Tensile specimen microstructure; after (c) 960/2 h/FC and (d) 1200/2 h/FC heat treatment. The inserts are an indication that the observed plane may or may not be parallel to the build direction, as the cutting for the metallographic preparation was done after the machining of the rounded tensile specimen.

homogenization (at 1200 °C for 2 h) and retained by a slow cooling rate (FC). As a result, α and β partitioning in a diffusion-controlled mode can occur, producing a lamellar microstructure of broad α and fine β in alternating lamellae packets, Fig. 7a. The β -phase is evident in the XRD profile in Fig. 5c. This microstructure seems to be dominant without changing throughout the strut section, Fig. 7b, mainly composed of plate-like α organized in α colonies and

α boundaries within the prior β grains. This microstructural coarsening leads to a drop in hardness and yield strength (Table 4), as expected.

The effective length of the α colonies was evaluated by the mean intercept length method for randomly oriented lines [21]. The lattice structures had a colony length of $110 \pm 20 \mu\text{m}$ while micrographs of the tensile specimens showed the length to be

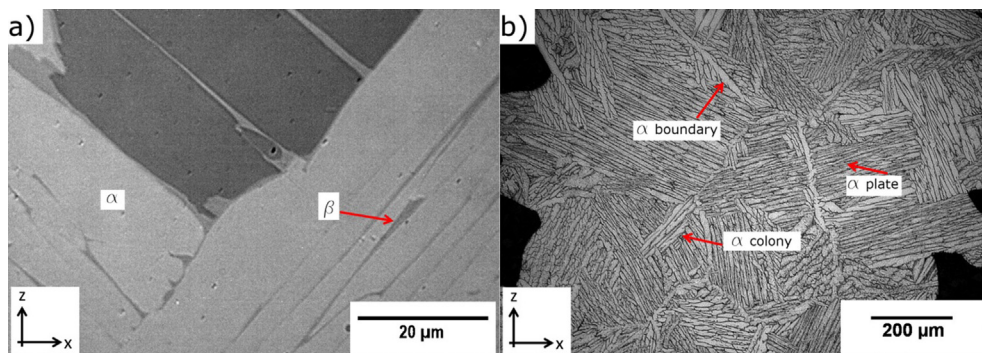


Fig. 7. Optical micrographs showing a) alternating α and β lamellae packets, b) equiaxed grains with plate-like α and α grain boundaries across the lattice strut member. The Z axis indicates the build direction.

$180 \pm 150 \mu\text{m}$ (no information about colony shape or morphology was obtained in either case). This suggests that the difference in size is related to the degree of recrystallization achieved in both volumes. This recrystallization effect has been seen on wire deposition additively manufactured structures after similar heat treatments [22], and also in microstructures after cold and hot working [23]. This is attributed, to some extent, to the high dislocation density created from going at high cooling rates from the β phase region giving an important driving force for the recrystallization process. As the “as-manufactured” EBM microstructure has been suggested to solidify at high cooling rates, therefore a strong tendency to recrystallize through a high dislocation density is latent.

As the heat treatment was applied to the specimens produced from a combination of material deposition strategies (hatching/contouring) further studies are necessary to investigate the generation of dislocations and their effects on deposited EBM Ti-6Al-4V materials. In this study, it is observed that for heat treatments above the β -transus temperature with FC applied to thin sections, as in the lattice samples, the excessive coarsening led to a small number of grains across the width of the struts (see image 7b), contributing to a decrease in mechanical properties discussed in the next section.

3.3. Compressive response

Compressive stress–strain curves of the 0.15 mm diameter Ti-6Al-4V lattice samples loaded axially in the EBM build direction are shown in Fig. 8. The sharp drop in strength represents the sudden failure of the sample under load.

The values for the collapse strength exhibited a systematic variation as a function of relative density, ρ_r , reporting: $23.7 \pm 2.4 \text{ MPa}$, $34.7 \pm 1.5 \text{ MPa}$, $180.2 \pm 14.3 \text{ MPa}$ for batches 1, 2 and 4 respectively, for batch 3 see Table 4. Once plotted in Fig. 9, the data was approximately fitted by a power law of exponent 1.58 determined by the least-squares method, in broad accordance with Eq. (1) albeit with a significantly higher constant of proportionality out of the range commonly reported for some cellular solids, e.g. metal foams [4]. For comparison, data from the diamond lattices (the struts replicating the interatomic bonds in the diamond crystal structure) is included in Fig. 9. It is seen that the cubic lattice examined here is significantly more mechanically efficient at comparable density. While the diamond lattices show a square fit close to a power of 2 (in agreement with the results reported by Körner et al. [24]), data from metal foams [6] display a lower value in accordance with bending-dominated models [3]. The mechanical resistance of cubic lattices along this orientation is good, despite the presence of minimally contribution of material in the struts aligned orthogonal to the loading direction, which contribute to the mass but to a low extent to the strength.

The expected load at failure (F^*) for the cubic lattices can therefore be calculated from equilibrium conditions, that is, from the force equally distributed through the vertical strut (f^*) times the number of vertical struts (n) contained in the squared area L^2 , see Eq. (3), leading to the failure stress in the lattice as shown in Eq. (4).

$$F^* = nf^* \quad (3)$$

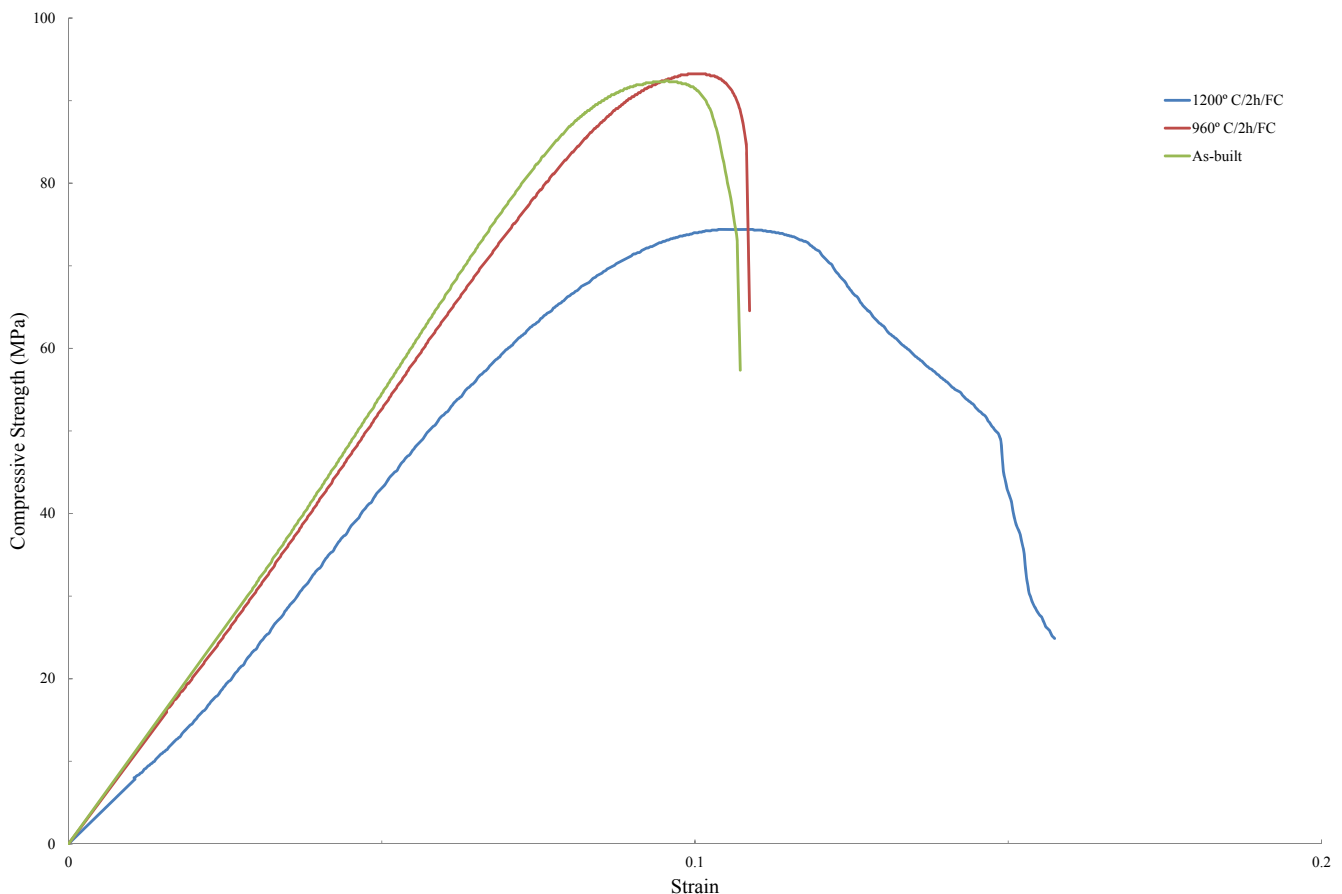


Fig. 8. An example stress–strain curve for lattices of each condition from batch 3.

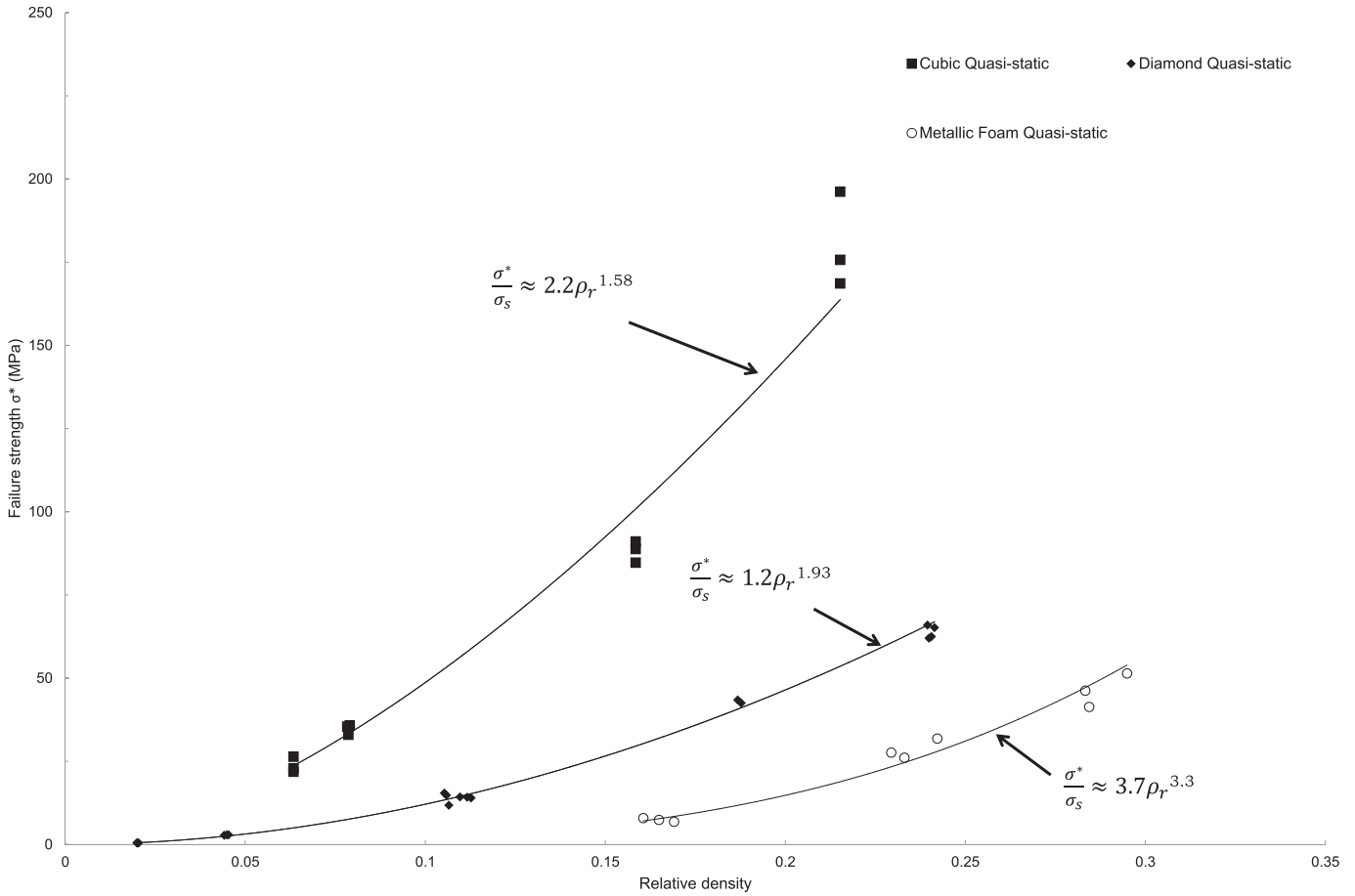


Fig. 9. Experimental compressive resistance with experimental relative density found in lattice samples. Results for diamond-like lattices and foams [6] are also shown for comparison.

$$\sigma^* = \sigma_s \frac{\pi}{4} \left[\frac{d}{l} \right]^2 \tag{4}$$

where σ^* , σ_s , d and l are the lattice failure stress, the parent material strength, the strut diameter and the unit cell length respectively. Substituting the relative density term (Eq. (2)) into Eq. (4), it gives:

$$\sigma^* = C \sigma_s \rho_r \tag{5}$$

where the constant $C = \frac{1}{3 - \left(\frac{4\sqrt{2}}{\pi}\right) \left(\frac{d}{l}\right)} \approx 0.286$ for the range studied

here. It has to be noted that the parent material yield strength (σ_s) was taken from the parameters measured in the tensile test on nominally dense additively manufactured material. This is a valid measure of the yield strength (in tension–compression) as it represents the initial departure from the linear elastic region, necking effects would mean that the test would not represent the later stages of compressive yielding [25]. Furthermore the assumption is made that struts fail by compressive yielding, not by buckling.

The experimental data fit well to this simple model based on pillar compression (Fig. 10) indicating that a) the initial yield is determined by pillar compression and not buckling at these strut lengths and diameters and secondly, that the yield strength of the bulk additively manufactured material is representative of that in the finer struts manufactured here. The proximity of the curve for

the onset of buckling approaches the compressive yielding curve for our struts at 0.81 mm (batch 1) diameter suggest that they are close to the buckling condition. Indeed pictures from the test (Fig. 11a and b) seem to confirm this as prior to failure, a type of cooperative buckling with linked nodes resisting the deformation seems to occur. However, if the strut is analysed locally, it can be seen that their length-to-diameter ratio decreases from node to node as the relative density increases. This becomes important for samples of batch 4 where a potential shear distortion can affect the total strength (σ^*). This is to be expected as shearing effects under compression are likely to be present if a length-to-diameter (l/d) is as low as 2.5 [25]. These conditions are close to those in the present case in batch 4 (1.8 mm diameter and 5 mm length) where SEM images show a transition in fracture, from a microvoid coalescence to a cleavage fracture see Fig. 12. Despite this transition in fracture and the flow of stresses determining the total lattice strength, the prediction based on yielding mechanisms suggests a satisfactory tendency for the range tested in this investigation.

The influence of the parent material properties is shown in Fig. 13. The intrinsic yield strength of the additively manufactured material (σ_s) was obtained from the bulk tensile tests (Table 4) and used to predict the compressive yielding of the lattice structures (σ^*) using Eq. (5). Error bars show the standard deviation in each batch. While the “as-manufactured” and 960° C/2h/FC lattice samples lie only 1% and 3% below the predicted strengths the structures treated at 1200° C/2 h/FC fall short by 11%.

The decreasing match of properties can be attributed to the effect of a coarse microstructure in narrow sections after heat treating

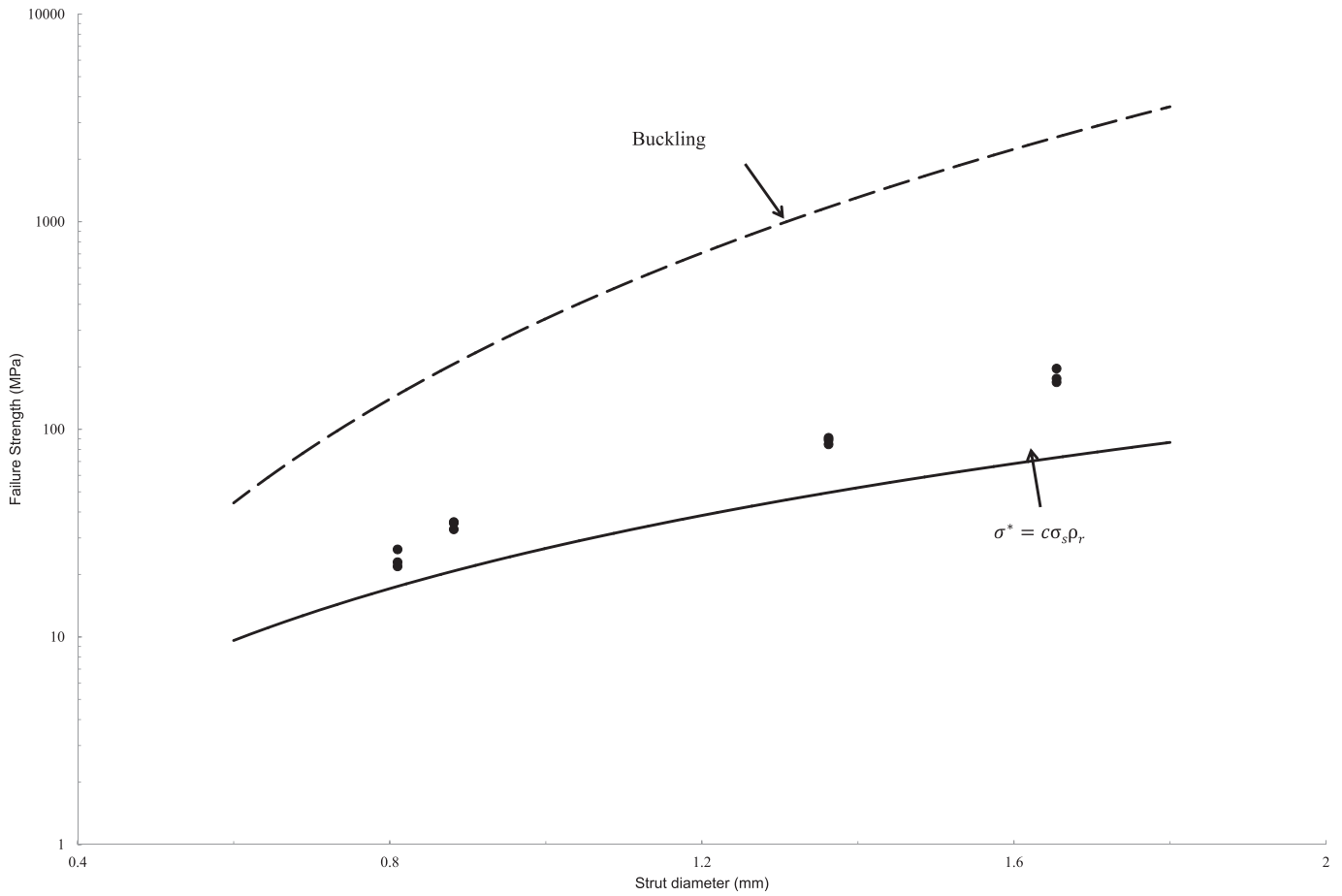


Fig. 10. Experimental data and analytical model prediction, for C see Eq. (5). The buckling failure mode was calculated as the height of one layer with nodes built in that cannot rotate therefore using a column effective length factor k of 0.5.

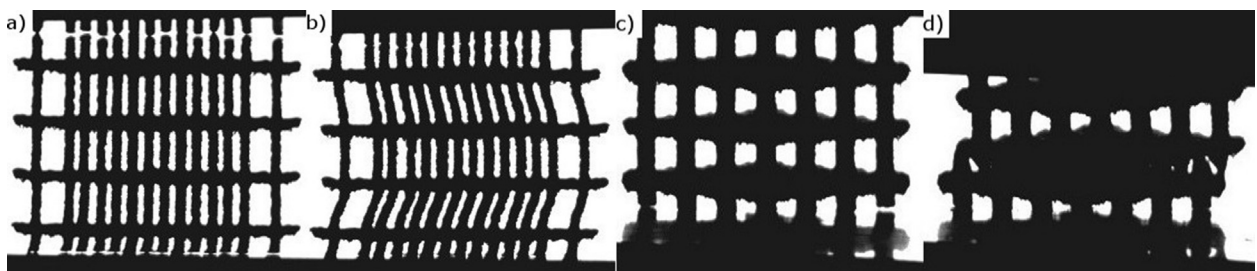


Fig. 11. Silhouette images from the video extensometer showing the pre-test and post-yield (pre-failure) forms of samples from batch 1 (a, b) and batch 4 (c, d).

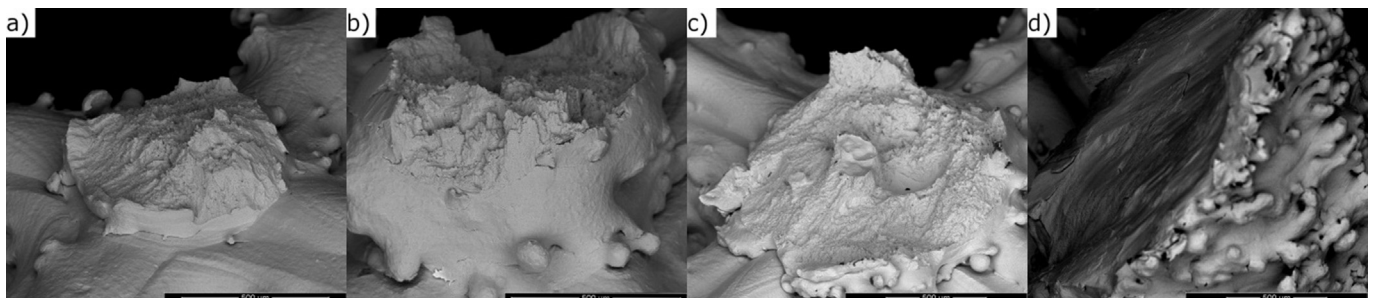


Fig. 12. SEM images of the node fractures for the compressed specimens, 0.8, 1, 1.5 and 1.8 mm in diameter respectively. A transition in fracture mechanism from a “dimpled” one to cleavage fracture at 1.8 mm can be seen.

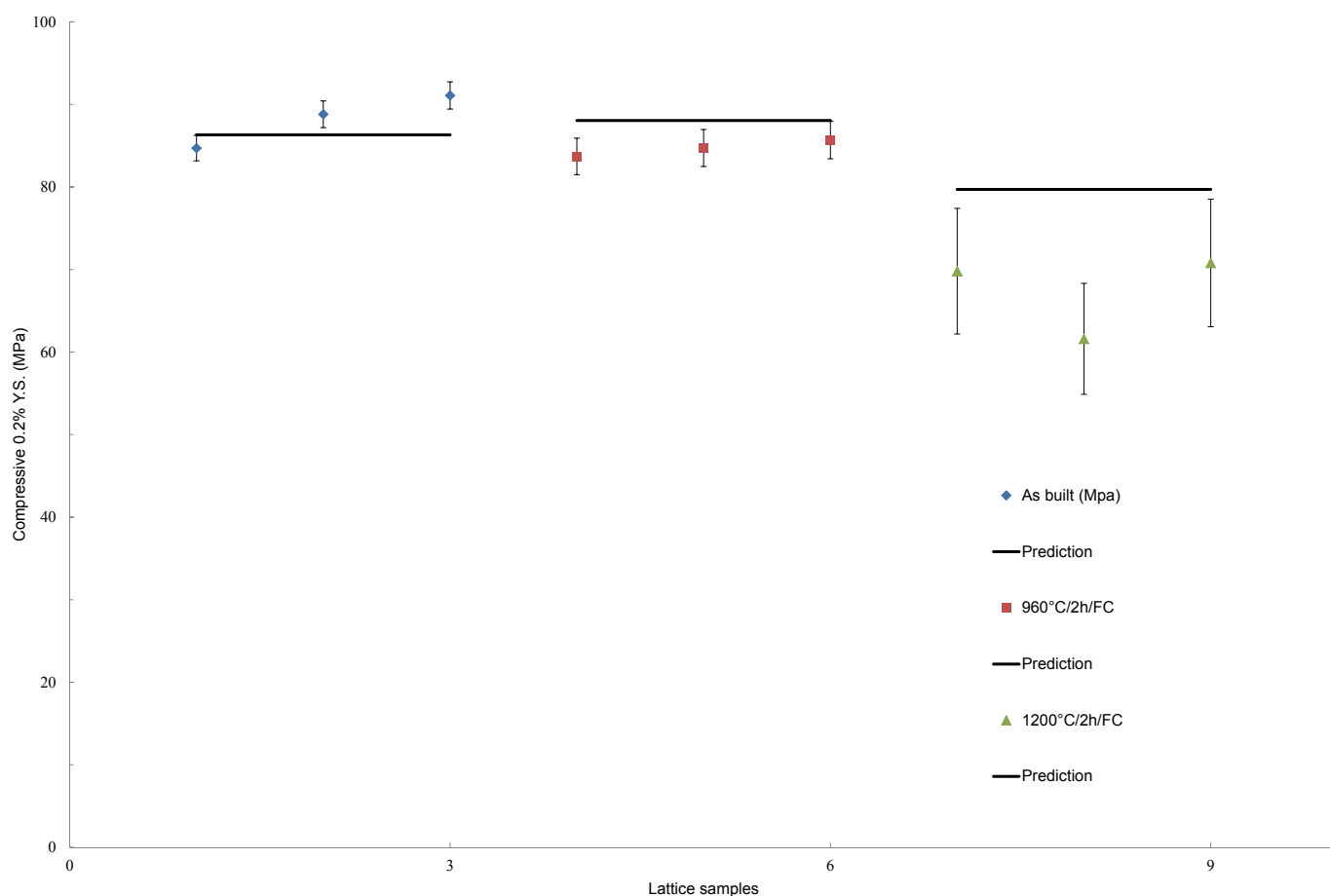


Fig. 13. Measured compressive yield strengths for the lattice structures compared to predictions based on 0.2% yield strength parent material data taken from nominally dense tensile samples.

above the β -transus temperature. Similar effects have been noted for annealed β in thin sheet form where the possible formation of a single β grain microstructure through the thickness could drastically affect the resistance [13]. It is not currently possible to identify up to what strut diameter the yield resistance can be affected by similar heat treatments for topologies presented here.

3.4. Strut cross sectional area

In order to assess the geometrical fidelity of EBM and the manufactures lattices, 7 single struts (named S1 to S7) were previously CT scanned by the authors [6] and analysed for this investigation. The range in cross-sectional areas of these struts (0.45–2 mm) aims to complement the range of struts previously discussed (0.8–1.8 mm) to build up the cubic lattices. The results are summarised in Table 5.

These observations show that fine struts ≤ 0.6 mm tend to be oversized while coarse struts ≥ 1 mm appear to be slight undersized (negative percentage). It should be pointed out that the set of single

struts were processed using the same beam parameters as for the lattices, and same powder size particles. Therefore, this over/under sizing can be attributed to the way the “weldtrack” was accommodated when the contouring and hatching took place while varying the strut size.

Further refinements to the analytical predictions as fitting parameters need to be included in expressions of the type of Eq. (5). For the range of lattices discussed here, only relatively undersized features are obtained, see Tables 2 and 5. Therefore, the overall plotted tendency in strength shown in Fig. 10 would be affected as $\sigma^* \approx \gamma C \sigma_s \rho_r$, where γ is the fitting parameter due to the discrepancy in area.

For the specimens presenting oversized dimensions, a similar situation has been reported previously [26] indicating that the EBM processing method with these beam parameters is incapable of reproducing features finer than $\sim 380 \mu\text{m}$ ($\sim 4\times$ the bigger particle diameter). The parameters used in this process produce a weldtrack width large enough to cover areas up to $600 \mu\text{m}$ with a single beam pass on solid Ti-6Al-4V substrates (see the single contour pass column in Fig. 14a). Fig. 14b and c shows redundant melting for full contouring and contouring plus hatching for areas of the same size. It is therefore expected that melting thin sections (with similar melt pool size and offset) out of the powder bed would pick up satellite particles around the periphery, oversizing areas above this value, see Fig. 14d. For undersized components however, the beam offset could be re-adjusted to achieve more accurate dimensions. However, the intrinsic pick up of particles around the edges of the solid may always be present causing deviations from the intended shape and size.

Table 5
Various strut specimens showing deviations in area and surface roughness Ra.

Sample	S1	S2	S3	S4	S5	S6	S7
STL diameter (mm)	0.4	0.6	1	1.2	1.5	1.8	2
Mean deviation in area (%)	52.9	18.5	-22.2	-18.0	-17.7	-15.5	-14.7
Ra (μm)	42.2	44.7	48.1	52.8	32.5	41.6	46.3

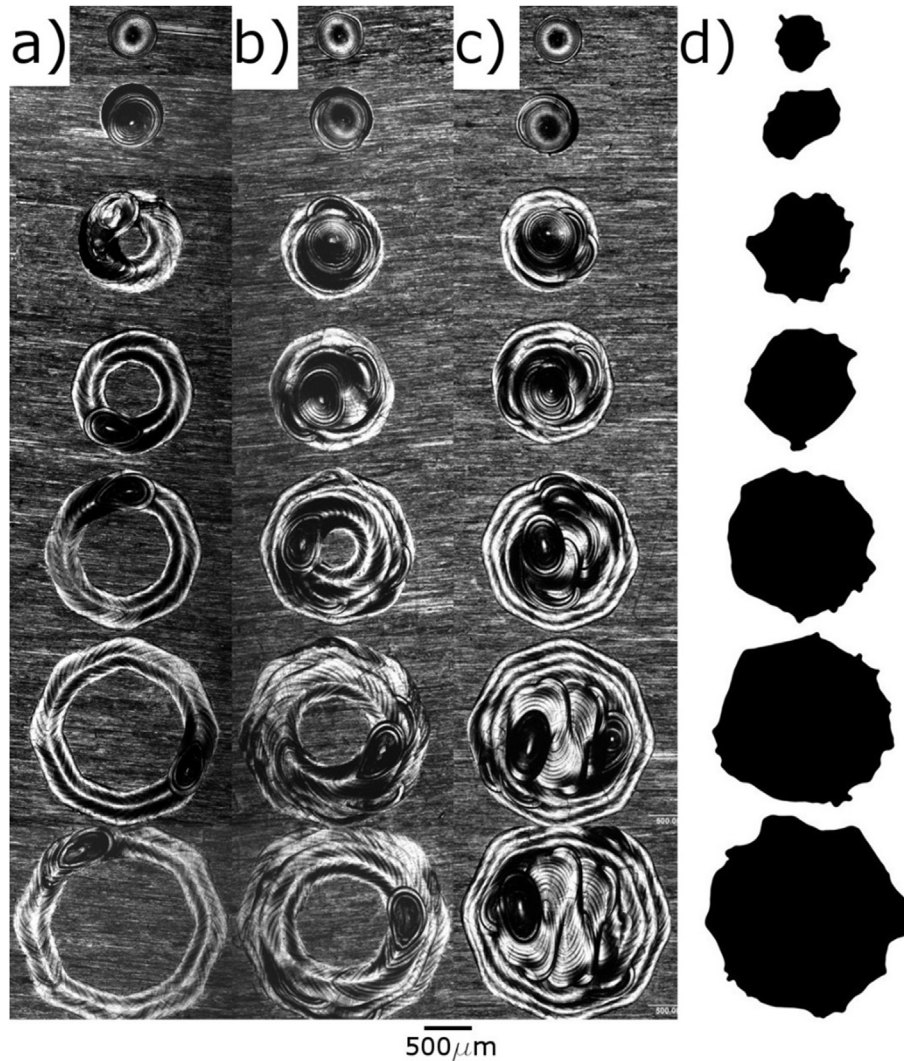


Fig. 14. Comparison of melted zones with strut diameter. (a) Shows one contour and (b) the full contouring region. (c) Shows contouring plus hatching stages. (d) Illustrates the corresponding CT strut slice selected at a random height.

In order to control the dimensions of EBM sections, especially avoiding oversized thin sections, prior adjustments in power input can be applied. From electron beam theory, a few models have been reported to predict the weldtrack width and depth in good agreement. Among those commonly used is the Rosenthal model [27], see Eq. (6).

$$T - T_0 = \eta q \frac{\eta q}{2\pi k R} \exp\left(\frac{-v}{2\alpha}(R + x)\right) \quad (6)$$

where T represents the melting material temperature, T_0 the material temperature, q the beam power, k is the thermal conductivity, α the thermal diffusivity, $R = \sqrt{(x^2 + y^2 + z^2)}$ the radial distance from the heat source, and v is the beam speed [12].

For the beam parameters used in this process, a single beam pass was performed on a pre-existing solid substrate to be further compared with the numerical solution, see Fig. 15. This single pass was carried out without preheating, which is present in the powder particles during the manufacturing of lattices, but the intention of the observation is to explore the shape formed in melting of thin sections.

The Fig. 15a shows the beam penetration highlighting the comparison with the numerical prediction. As mentioned, the

experimental depth-to-width ratio is close to the ideal proposed by the model where the radius R is of circular shape along the Z axis. It can therefore be seen that a good agreement between the model and the experimental results exists. It is worth mentioning that despite the possible effects of focus offset and the electron beam efficiency [14], the power input could further be investigated to obtain lower penetrations and as a result allow the formation of thinner melted sections.

3.5. Internal defects and surface roughness

As mentioned earlier, the analysis carried out in previous investigation [6] was focused on the volume fraction of defects; here we look carefully at the distribution of defects in relation to the manufacturing scheme because previous work suggests that the pattern of voids is related to the scan sequence [9]. This arises because the viscous forces within the liquid titanium trap pre-existing gas bubbles which arrange in patterns determined by the electron beam pattern. For each strut, the variation in pore volume fraction moving in from the surface in the x - y plane was quantified. This indicates that the voids are concentrated in rings (see inset Fig. 16). Consequently the radial distance of the porosity is shown in

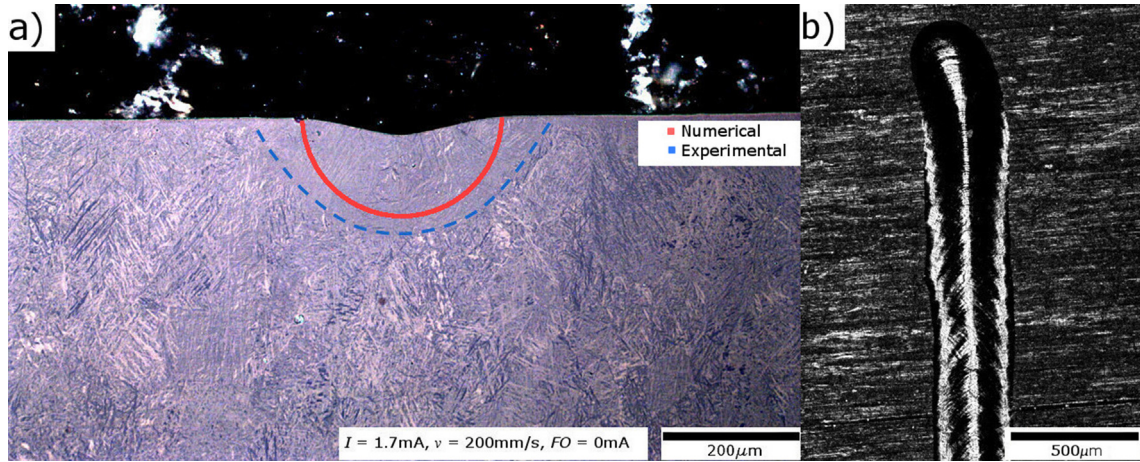


Fig. 15. A single beam pass (weldtrack) on a pre-existing solid Ti-6Al-4V plate showing (a) experimental and numerical beam depth penetration and, in (b) the beam width. With a width-to-depth ratio of 0.55, it shows a good agreement to the ideal circular shape by the point heat source model. The numerical prediction was obtained using an efficiency $\eta = 0.8$, 7 W/mK of thermal conductivity, $T_m = 1660$ and 580 J/kg K of heat capacity [13].

Fig. 16 for the struts of different diameters. It is evident that the porosity appears to be concentrated at two distances; one approximately 50 μm from the surface and another at 400 μm in cases where the strut is sufficiently thick.

In order to interpret these results it is helpful to layout the scan schemes used to fill struts of different diameters (Fig. 14). It is noteworthy that the porosity 50 μm from the surface coincides with the offset from the CAD contour at which the hatching process was commenced, while the 400 μm distance is approached by the thickness of a single weld track in this material. For the four most slender struts, the cross sectional area is not sufficient for a well-defined contouring region, Fig. 14b, whereas thicker struts allow the contouring and the hatching regions to be clearly distinguished, Fig. 14c.

On the other hand, the size deviations from the beam path across the random arrangement of powder particles and melting strategies, generates roughness. To report this evidence, Arithmetic average values (Ra) was obtained from the visualization analysis. It can be seen that the roughness Ra is found in a range of $44 \pm 6.3 \mu\text{m}$, which is close to the order of the smaller powder particle size. As mentioned earlier it is suggested that particles around the perimeter can be attached, leaving their trace on the surface defining the roughness. This effect can be compared with similar results published by Karlsson et al. [28] where two fractions of powder size were employed to melt components in EBM systems where the smaller particles left a different roughness with higher average peak to valley ratio due to more particles being attached to the surface.

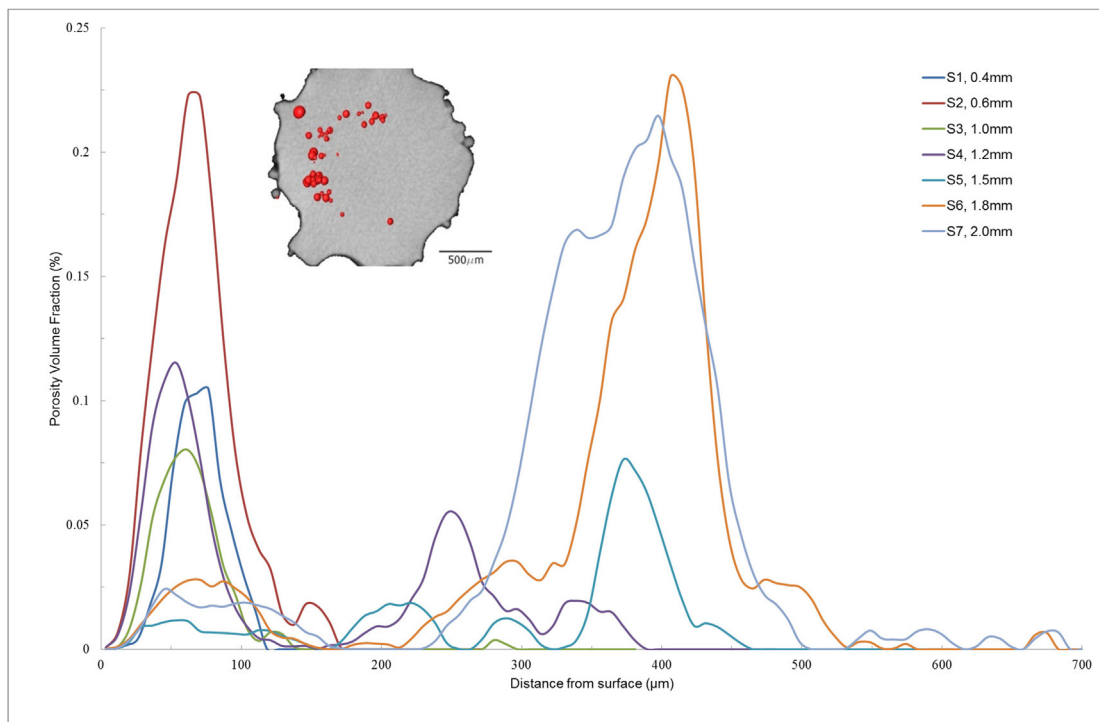


Fig. 16. Porosity volume fraction with the distance from the outer contour for strut of different diameters. The porosity in the 2 mm diameter strut is shown inset projected onto a strut cross section.

It is perhaps surprising that the presence of these defects seems to have little influence on the lattice strength, with the experimental results in good agreement with the simple model prediction. Of course failure as against the onset of yielding is much more likely to be sensitive to this fraction of defects and further research is needed both to improve dimensional accuracy (and analytical or numerical models to account this for) but also to investigate the knockdown on ultimate properties due to such defects.

4. Conclusions

Electron Beam Melting (EBM) and CAD tools have successfully been applied to additively manufacture fine cubic lattice structures using Ti-6Al-4V 45–100 μm prealloyed powder. In this paper the microstructure and dimensional accuracy of the as-manufactured lattices have been investigated for a set of lattices having the same morphology except for the strut diameter which was varied systematically. It was found that heat treatment below the β -transus had relatively little effect on the microstructure or properties such that the as manufactured state can be considered as being in the annealed condition. Heat treatment above the β transus had a much more marked effect significantly coarsening the structure and leading to coarse alternating α and β lamellae packets and α at the prior grain boundaries. While the former treatment had very little effect on the mechanical performance the higher heat treatment lowered the compressive yield stress by approximately 11%.

The compressive yield behaviour could be predicted for all the diameters manufactured simply in terms of the compressive plastic deformation of the aligned struts rather than the onset of buckling or shearing, though these may well lead to ultimate failure. The properties of the AM struts within the fine lattices were approximately those of bulk additively manufactured material. Intrinsic fully entrained defects are also seen; for aligned along the build direction these were small and located primarily in rings associated with the EB scan profile. As one might expect given the redundancy of the horizontal struts the compressive yield strength was little affected by defects in these struts. Much larger surface breaking defects were found for struts lying normal to the build direction. The minimum weld-track size was experimentally and numerically identified to be 176 and 148 μm in depth respectively with a depth-to-width ratio of 0.55. This produced a beam pass of the order of 300 μm oversizing small features (struts of 0.4 and 0.6 mm nominal diameter) when a contour around the strut diameter was applied. The area deviations were parametrically identified up to 52% for oversized component however, as the beam parameters are able to reproduce thinner sections, this issue could potentially be corrected in future. Raw materials and deposition strategies are suggested to be further investigated to refine accuracy. Additionally, the surface roughness is significant (close to the smaller particle size) and is believed to be due to the entrainment of particles on the periphery of the external contour specified by the scanning scheme.

Acknowledgements

One of the Authors (Hernández-Nava E.) would like to acknowledge the support of a studentship provided by CONACYT and Roberto Rocca Education Program. The authors Tammam-Williams S. and Smith C. acknowledge funding from EPSRC for the Advanced Metallic Systems CDT (EP/L016273/1) at the universities of Manchester and Sheffield. The Manchester Henry Moseley X-ray Imaging Facility was funded in part by the EPSRC (grants EP/F007906/1, EP/F001452/1 and EP/I02249X/1).

References

- [1] R. Goodall, A. Mortensen, Porous metals, in: fifth ed., in: D. Laughlin, K. Hono (Eds.), *Physical Metallurgy*, Vol. 7, Elsevier, 2014, pp. 2399–2595.
- [2] Y. Sun, T. Lowe, S.A. McDonald, Q.M. Li, P.J. Withers, In-situ investigation and image-based modelling of aluminium foam compression using micro X-ray computed tomography, in: *Visual Computing: Scientific Visualization and Imaging Systems*, Patent, 2014, pp. 189–197.
- [3] M.F. Ashby, The properties of foams and lattices, *Philos. Trans. A. Math. Phys. Eng. Sci.* 364 (1838) (Jan. 2006) 15–30.
- [4] M.F. Ashby, A. Evans, N.A. Fleck, L.J. Gibson, J.W. Hutchinson, H.N.G. Wadley, *Metal Foams. A Design Guide*, Butterworth-Heinemann, 2000.
- [5] L. Yang, O. Harrysson, H. West, D. Cormier, “Compressive properties of Ti–6Al–4V auxetic mesh structures made by electron beam melting, *Acta Mater.* 60 (8) (May 2012) 3370–3379.
- [6] E. Hernández-Nava, C.J. Smith, F. Derguti, S. Tammam-Williams, F. Léonard, P.J. Withers, I. Todd, R. Goodall, The effect of density and feature size on mechanical properties of isostructural metallic foams produced by additive manufacturing, *Acta Mater.* 85 (Feb. 2015) 387–395.
- [7] C.J. Smith, M. Gilbert, I. Todd, and F. Derguti, Application of layout optimization to the design of additively manufactured metallic components, *Struct. Multidiscip. Optim.*, (Accepted).
- [8] I. Gibson, D.W. Rosen, B. Stucker, *Rapid Manufacturing Technologies, Rapid Prototyping to Direct Digital Manufacturing*, Springer, 2010.
- [9] S. Tammam-Williams, H. Zhao, F. Léonard, F. Derguti, I. Todd, P.B. Pragnell, XCT analysis of the influence of melt strategies of defect population in titanium components manufactured by selective electron beam melting, *Mater. Characterisation* 102 (2015) 47–61.
- [10] C. Smith, F. Derguti, E. Hernandez Nava, M. Thomas, S. Tammam-Williams, S. Gulizia, D. Fraser, I. Todd, Dimensional accuracy of Electron Beam Melting (EBM) additive manufacture with regard to weight optimized truss structures, *J. Mater. Process. Technol.* 229 (2016) 128–138.
- [11] N. Taniguchi, M. Ikeda, I. Miyamoto, T. Miyasaki, *Energy Beam Processing of Materials: Advanced Manufacturing Using Various Energy Sources*, Oxford University Press, 1989.
- [12] J.W. Elmer, W.H. Giedt, T.W. Eagar, “The Transition from Shallow to Deep Penetration during Electron Beam Welding, *Weld. J.* (1990) 1167–1176 no. May.
- [13] G. Welch, R. Boyer, E.W. Collings (Eds.), *Material Properties Handbook: Titanium Alloys*, second ed., ASM International, Materials Park, OH, USA, 1998.
- [14] S.S. Al-Bermani, M.L. Blackmore, W. Zhang, I. Todd, The origin of microstructural diversity, texture, and mechanical properties in electron beam melted Ti-6Al-4V, *Metall. Mater. Trans. A* 41 (13) (Aug. 2010) 3422–3434.
- [15] N. Otsu, A threshold selection method from gray-level histograms, *IEEE Trans. Syst. Man. Cyber.* 19 (1979) 62–66.
- [16] L.E. Murr, K.N. Amato, S.J. Li, Y.X. Tian, X.Y. Cheng, S.M. Gaytan, E. Martinez, P.W. Shindo, F. Medina, R.B. Wicker, Microstructure and mechanical properties of open-cellular biomaterials prototypes for total knee replacement implants fabricated by electron beam melting, *J. Mech. Behav. Biomed. Mater.* 4 (7) (Oct. 2011) 1396–1411.
- [17] T. Ahmed, H.J. Rack, Phase transformations during cooling in α + β titanium alloys, *Mater. Sci. Eng. A* 243 (1–2) (1998) 206–211.
- [18] L. Wang, S. Felicelli, Influence of process parameters on the phase transformation and consequent hardness induced by the LENS™ process, in: *TMS Annual Meeting & Exhibition*, 2007.
- [19] G. Lütjering, J.C. Williams, *Titanium. Engineering Materials and Processes*, second ed., Springer, 2007.
- [20] L.E. Murr, S.M. Gaytan, F. Medina, H. Lopez, E. Martinez, B.I. Machado, D.H. Hernandez, L. Martinez, M.I. Lopez, R.B. Wicker, J. Bracke, Next-generation biomedical implants using additive manufacturing of complex, cellular and functional mesh arrays, *Philos. Trans. A. Math. Phys. Eng. Sci.* 368 (1917) (Apr. 2010) 1999–2032.
- [21] J. Tiley, T. Searles, E. Lee, S. Kar, R. Banerjee, J.C. Russ, H.L. Fraser, Quantification of microstructural features in α/β titanium alloys, *Mater. Sci. Eng. A* 372 (1–2) (May 2004) 191–198.
- [22] E. Brandl, A. Schoberth, C. Leyens, Morphology, microstructure, and hardness of titanium (Ti-6Al-4V) blocks deposited by wire-feed additive layer manufacturing (ALM), *Mater. Sci. Eng. A* 532 (Jan. 2012) 295–307.
- [23] R. Ding, Z.X. Guo, Microstructural evolution of a Ti–6Al–4V alloy during β -phase processing: experimental and simulative investigations, *Mater. Sci. Eng. A* 365 (1–2) (Jan. 2004) 172–179.
- [24] P. Heintz, C. Körner, R.F. Singer, Selective electron beam melting of cellular titanium: mechanical properties, *Adv. Eng. Mater.* 10 (9) (Sep. 2008) 882–888.
- [25] G.E. Dieter, Mechanical Behavior Under Tensile and Compressive Loads, in: H. Kuhn, D. Medlin (Eds.), *ASM Handbook, 10th ed. Mechanical Testing and Evaluation*, Volume 8, ASM International, 1986, pp. 258–259.
- [26] W. van Grunsven, E. Hernández-Nava, G. Reilly, R. Goodall, Fabrication and mechanical characterisation of Titanium lattices with graded porosity, *Metals* 4 (3) (2014) 401–409.
- [27] D. Rosenthal, The theory of moving sources of heat and its application to metal treatments, *Trans. ASME* 11 (43) (1946) 849–866.
- [28] J. Karlsson, A. Snis, H. Engqvist, J. Lausmaa, Characterization and comparison of materials produced by electron beam melting (EBM) of two different Ti-6Al-4V powder fractions, *J. Mater. Process. Technol.* 213 (12) (2013) 2109–2118.